HAL open science

Magnetic activity on AB Doradus: temporal evolution of star-spots and differential rotation from 1988 to 1994

S. V. Jeffers, J.-F. Donati, A. Collier Cameron

To cite this version:

S. V. Jeffers, J.-F. Donati, A. Collier Cameron. Magnetic activity on AB Doradus: temporal evolution of star-spots and differential rotation from 1988 to 1994. Monthly Notices of the Royal Astronomical Society, 2007, 375, pp.1492. 10.1111/J.1365-2966.2006.11154.X . hal-00138870

HAL Id: hal-00138870

https://hal.science/hal-00138870v1

Submitted on 18 Jan 2021

HAL is a multi-disciplinary open access archive for the deposit and dissemination of scientific research documents, whether they are published or not. The documents may come from teaching and research institutions in France or abroad, or from public or private research centers.

L'archive ouverte pluridisciplinaire **HAL**, est destinée au dépôt et à la diffusion de documents scientifiques de niveau recherche, publiés ou non, émanant des établissements d'enseignement et de recherche français ou étrangers, des laboratoires publics ou privés.

Mon. Not. R. Astron. Soc. **375,** 567–583 (2007) doi:10.1111/j.1365-2966.2006.11154.x

Magnetic activity on AB Doradus: temporal evolution of star-spots and differential rotation from 1988 to 1994

S. V. Jeffers,[1,2]★ J.-F. Donati[1] and A. Collier Cameron[2]

[1]*Laboratoire d'Astrophysique Toulouse-Tarbes, Observatoire Midi-Pyrénées, 14 avenue Edouard Belin, F-31400 Toulouse, France*
[2]*School of Physics and Astronomy, University of St Andrews, North Haugh, St Andrews, Fife KY16 9SS*

Accepted 2006 October 5. Received 2006 September 22; in original form 2005 December 8

Downloaded from https://academic.oup.com/mnras/article/375/2/567/1442930 by guest on 15 December 2020

ABSTRACT

Surface brightness maps for the young K0 dwarf AB Doradus are reconstructed from archival data sets for epochs spanning from 1988 to 1994. By using the signal-to-noise ratio enhancement technique of least-squares deconvolution, our results show a greatly increased resolution of spot features than obtained in previously published surface brightness reconstructions. These images show that for the exception of epoch 1988.96, the star-spot distributions are dominated by a long-lived polar cap, and short-lived low to high-latitude features. The fragmented polar cap at epoch 1988.96 could indicate a change in the nature of the dynamo in the star. For the first time we measure differential rotation for epochs with sufficient phase coverage (1992.05, 1993.89, 1994.87). These measurements show variations on a time-scale of at least 1 year, with the strongest surface differential rotation ever measured for AB Dor occurring in 1994.86. In conjunction with previous investigations, our results represent the first long-term analysis of the temporal evolution of differential rotation on active stars.

Key words: line: profiles – stars: activity – stars: individual: AB Dor – stars: rotation – stars: spots.

1 INTRODUCTION

Solar-type stars exhibit signatures of magnetic activity that are assumed to be based on dynamo mechanisms operating in the star's outer convective zone. The detailed workings of the generation and amplification mechanisms of the stellar dynamos are still poorly understood as a result of the complex physics involved in theoretical models, and the lack of observational constraints. However, it is widely accepted that differential rotation and convection are essential ingredients of common theoretical amplification models (Parker 1955; Leighton 1964; Babcock 1965; Leighton 1969).

Differential rotation results from the interplay of rotation and convection, which leads to a redistribution of heat and angular momentum inside the convection zone. The thermal and density profiles of convective motions produce a dependence of differential rotation on both stellar latitude and radius. It is a key process in the cyclic activity of the stellar dynamo being the process through which poloidal–toroidal field conversion occurs. To date there have been numerous measurements of differential rotation on rapidly rotating cool stars, summarized by Barnes et al. (2005), that show a steady increase in the magnitude of differential rotation towards earlier spectral types, consistent with the theoretical predictions of Rüdiger & Küker (2002). In addition, helioseismology reveals a differential rotation profile that varies with radius and latitude and is caused by the presence of an intense turbulence in the solar convention zone, which is driven by Reynolds stresses (Brun & Toomre 2002).

Several methods have been used to measure differential rotation. The methods of Gray (1977), Bruning (1981) and Reiners & Schmitt (2002) use Fourier analysis to detect differential rotation through line profile analysis. These methods are only applicable to stars that do not exhibit large cool star-spots as they distort the shape of the line profile. Other methods reconstruct surface brightness images over a time period and then trace surface features to ascertain how their rotation periods are dependant on latitude. Examples include, the cross-correlation method used by Donati & Collier Cameron (1997) on AB Dor to obtain the first differential rotation measurement for a star other than the Sun. This method measures the amount of rotational shear as a function of latitude by cross-correlating belts of equal latitude. The sheared-image method extends this to include a solar-like differential rotation law into the image reconstruction process, where the rotation rate is allowed to vary smoothly with latitude on an image grid (Donati et al. 2000).

The temporal evolution of differential rotation can be determined by measurements over several epochs as shown for AB Dor by Collier Cameron & Donati (2002). In this work, a matched-filter analysis method was used to track individual spot features in the trailed spectrograms. The temporal evolution of differential rotation on AB Dor has also been confirmed by Donati et al. (2003b), through

★E-mail: s.v.jeffers@astro.uu.nl

© 2007 The Authors. Journal compilation © 2007 RAS

Table 1. Journal of observations for AB Dor showing the observed spectral domain, pixel size, resolution and the instrument used for each epoch.

Epoch	Spectral domain (nm)	Pixel size (km s^{-1})	Resolution	Telescope/spectrograph
1988 December 16, 19	605.9249–724.4182	2.7	56 000	AAT/UCL
1988 December 21	581.0809–673.5818	4.6	27 000	ESO(3.6 m)/CASPEC
1992 January 18, 19, 20	498.2082–708.8381	2.42	51 100	AAT/UCL
1992 December 14	452.9687–688.6151	2.98	33 600	AAT/UCL
1993 November 23, 24, 25	479.6900–751.7410	2.98	33 600	AAT/UCL
1994 November 15, 16, 17	551.0686–792.9818	3.56	26 600	CTIO

Table 2. Journal of observations showing Julian Dates (+245 0000), phase coverage, S/N of the data set, and the number of lines used in deconvolution.

Epoch	Julian Date	Phase range	S/N	No. of lines	References
1988.96	7511.7607–7514.8768	−0.37 to −0.174 : 0.381–0.672	70–100	80	Collier Cameron et al. (1990)
1988.97	7516.5617–7518.8339	0.961–1.517	280–300	290	Collier Cameron et al. (1990)
1992.05	8639.9234–8642.2515	0.127–0.782 : 0.038–0.722 : 0.98–0.628	50–110	945	Collier Cameron & Unruh (1994)
1992.95	8970.9158–8971.2737	0.092–0.766	110–180	2134	Collier Cameron (1995)
1993.89	9314.9249–9317.2631	−0.656 to 0.034 : −0.266 to 0.918 : 0.175–0.886	56–95	1515	Unruh et al. (1995)
1994.87	9671.5421–9673.8443	0.087–0.591 : 0.698–0.525 : 0.604–0.555	160–250	990	Collier Cameron et al. (1999)

the use of the sheared-image method, though not for the same epochs as Collier Cameron & Donati (2002).

In this paper we extend the epochs for which differential rotation has been measured using the sheared-image method, by processing archival AB Dor data for epochs 1988 December, 1992 January, 1993 November and 1994 November (presented in Section 2). This is the first time that surface brightness images have been reconstructed from composite profiles computed from these data sets using the signal-to-noise ratio (S/N) enhancement technique least-squares deconvolution (LSD) (presented in Sections 3 and 4). Finally, we measure differential rotation for each epoch with sufficient rotational phase coverage (presented in Section 5) and discuss the implications of our results in Section 6.

2 OBSERVATIONS AND DATA MODELLING

The details of the instrument configuration and observing procedures used to secure the six data sets are summarized in Table 3. We refer the reader to the publications listed in Table 2 for further details.

2.1 Data reduction

All frames were processed with ESPRIT, a dedicated package for the optimal extraction of echelle spectroscopic observations. First a 3D fit of the bias frame is subtracted from the flat-field and arc frames. Each order of the raw echelle frame is then located and traced using cross-correlations with a user-defined reference profile. A linear or 2D fit to the shape of the arc lines provides the slit direction. Deviations from the slit direction are averaged over all orders provide the mean slit shape.

The first step in the wavelength calibration procedure is to obtain an accurate identification of calibration lines. To start, the user specifies the order numbers, and approximate values for the wavelength of the first pixel and pixel size. This information is used to determine the location of lines from a calibration line list. A quadratic dispersion polynomial is then determined and used to calibrate the remaining orders. The final dispersion relation is obtained by fitting a 2D polynomial to the pixel positions and corresponding wavelengths of all lines simultaneously. The comprising dimensions of the polynomial fit are: one dimension to fit the dispersion relation of each order and one dimension to fit its variation from one order to the next.

Table 3. Radial velocity measurements for each epoch of this analysis with previously published values for epochs after 1994.

Epoch	Radial velocity (km s^{-1})
1988 December 16 and 19	32.2
1992 January	31.2
1992 December	28.8
1993 November	29.7
1994 November	29.9
1995 December	31.4
1996 December	31.4
1998 January	31.5
1998 December	31.6
1999 December	31.8
2000 December	32.1
2001 December	32.7
2002 December	32.9

Pixel-to-pixel sensitivity differences are removed by dividing each pixel in the stellar frame by the corresponding pixel in the flat-field. A 2D polynomial fit to the interorder background is subtracted from the stellar frame. All pixels that deviate from the average intensity of the order (i.e. cosmic rays) are removed. The optimal extraction of Marsh (1989) is then implemented. The continuum is automatically fitted firstly by using a high-degree 1D polynomial, and then by a 2D polynomial to identify any systematic trends in the continuum's shape. A more detailed description of this package is given by Donati & Collier Cameron (1997).

2.2 Least-squares deconvolution

LSD is a method for combining the rotation profiles of thousands of spectral lines in an optimally weighted manner (Donati et al.

Downloaded from https://academic.oup.com/mnras/article/375/2/567/1442930 by guest on 15 December 2020

1997). It uses a weighted least squares algorithm to compute the line-broadening profile which, when convolved with the known pattern of photospheric absorption lines in a stellar spectrum, optimizes the chi-squared fit to the data. The list of spectral lines is obtained from the LTE model atmospheres of Kurucz (1993) for $T_{\rm eff} = 5000$ K and $\log g = 4.5$, where features with a relative central depth of at least 40 per cent of the local continuum flux are used. The total number of lines used for each epoch is shown in Table 2.

It can be shown that the enhancement in S/N is equivalent to either an optimally weighted stacking of the profiles, or to cross-correlation with the line pattern, scaling as the square root of the number of lines used. It has the advantage, however, that sidelobes caused by blends are automatically eliminated from the composite profile, giving a clean profile surrounded by flat continuum. LSD conserves the shape of the rotational profile, implying that any deviations in this profile can be interpreted as brightness inhomogeneities on the stellar surface.

3 RADIAL VELOCITY CORRECTION

3.1 Telluric line alignment

Telluric lines are used to correct for small shifts in the spectrograph during the night, that is, from Dewar refill and the thermal and mechanical relaxation of spectrograph's components, as they are only present in the Earth's atmosphere and are therefore at zero radial velocity. We use the procedure of Donati et al. (2003a) in this analysis. First the composite profile of telluric absorption lines in each stellar spectrum is computed using LSD, with a line mask comprising the wavelengths and relative strengths of known telluric features (mainly of water) in the observed spectral region. The instrumental velocity of the composite telluric profile is then measured and used to define the zero-point of the velocity scale. Each stellar profile is then shifted by the measured instrumental velocity before applying heliocentric velocity corrections.

3.2 Radial velocity results

The radial velocity derived for each epoch is tabulated in Table 3, where over the time-span of our observations there is a variation of 3.4 km s^{-1}. The change in radial velocity reflects the orbital motion of AB Dor predominantly due to the presence of its closest companion, AB Dor C (Close et al. 2005). AB Dor C is a low-mass object (0.09 M$_\odot$) first detected by Guirado et al. (1997), which orbits AB Dor A at a separation of 0.156 arcsec. In addition to AB Dor C, AB Dor is known to have a wide companion AB Dor B (Vilhu, Gustafsson & Walter 1991; Martin & Davey 1995) which is itself a close binary system, and is separated from AB Dor A by a distance of 9.09 ± 0.01 arcsec.

The AB Dor A and C orbital solution has been determined by Close et al. (2005), where the parameters that define the reflex orbit of AB Dor A are fitted by: period = 11.75 ± 0.25 yr, semimajor axis = 0.032 ± 0.002 arcsec, eccentricity = 0.59 ± 0.03, periastron passage at 1991.8 ± 0.2, inclination = 67° ± 3°, $\Omega = 132° \pm 2°$, $\omega = 107° \pm 7°$. The orbital solution is shown in Fig. 1 to fit the data points within the error bars and to follow the decrease in radial velocity at periastron (epoch 1991.8). The error is approximately 0.5 km s^{-1} for the epochs of this work and 0.3 km s^{-1} for epochs after 1995, and results from broad and time variable stellar lines. The exceptions are the radial velocity measurements of epochs 1992.95, 1993.89 and 1994.87, but the good fits to the line profile shown in Figs 5 and 6 for epoch 1992.05, Fig. 9 for epoch 1992.95 and Figs 10 and 11 for epoch 1993.89, exclude any additional measurement errors. More empirical data points will help to constrain the errors of the orbital solution.

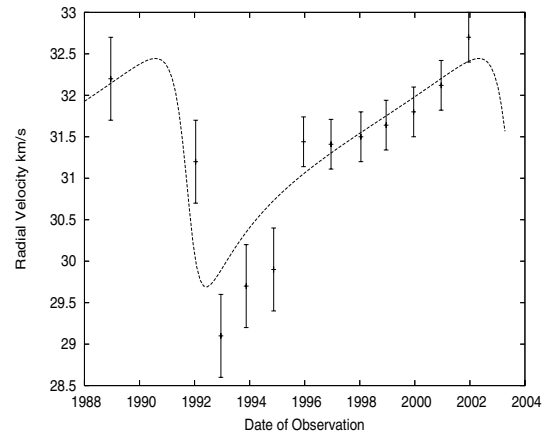

Figure 1. The orbital solution of Close et al. (2005) for the reflex orbit of AB Dor A. Also plotted are the empirically derived radial velocity values for AB Dor as determined by this analysis (epochs 1988–1994), The orbital solution includes an offset in the *y*-axis of 31.37 km s^{-1} that corresponds to the radial velocity of the binary system, which was determined by χ^2 minimization. The χ^2 obtained for this solution is 6.023.

4 SURFACE IMAGE RECONSTRUCTION

The surface brightness images are reconstructed using the maximum entropy code of Brown et al. (1991) and Donati & Brown (1997). The brightness model that is incorporated in this code is the 'spot occupancy' model of Collier Cameron (1992), where each point on the stellar surface is quantified by the local fraction of the stellar surface occupied by spots. The range of spot occupancy is from 0, where there are no spots present, to 1, where there is maximum spottedness.

The imaging parameters that are used in this work for AB Dor are stellar axial inclination, $i = 60°$, the projected equatorial rotation velocity, $v \sin i = 89$ km s^{-1} and the photospheric and spot temperatures, respectively, 5000 and 3500 K (Donati et al. 2003a). All data sets are phased according to the ephemeris of Innis et al. (1988); HJD = 244 4296.575 + 0.514 79 E. LSD profiles of slowly rotating standard stars (GL 176.3 and GL 367) are used as template profiles that represent the contribution of the photosphere and the spot to the shape of the intrinsic line profile.

4.1 Results

All data sets provide good sampling of the rotational cycle of AB Dor. The maximum entropy images are structurally very similar with a polar cap and/or high-latitude spots, and with varying degrees of low-latitude spots. The longitude resolution is approximately 3° at the equator and the size of the smallest features in latitude.

The maximum entropy fits and the reconstructed surface brightness image for 1988 December are respectively shown in Figs 2, 3 and 4. It shows high-latitude spots that dominate over a weak polar cap and a dearth of low-latitude spot coverage. These sets were originally observed with the aim of detecting circumstellar clouds on AB Dor using Hα, Ca II H and K, and Mg II h and k lines Collier Cameron et al. (1990). The most striking feature of this data set is

Downloaded from https://academic.oup.com/mnras/article/375/2/567/1442930 by guest on 15 December 2020

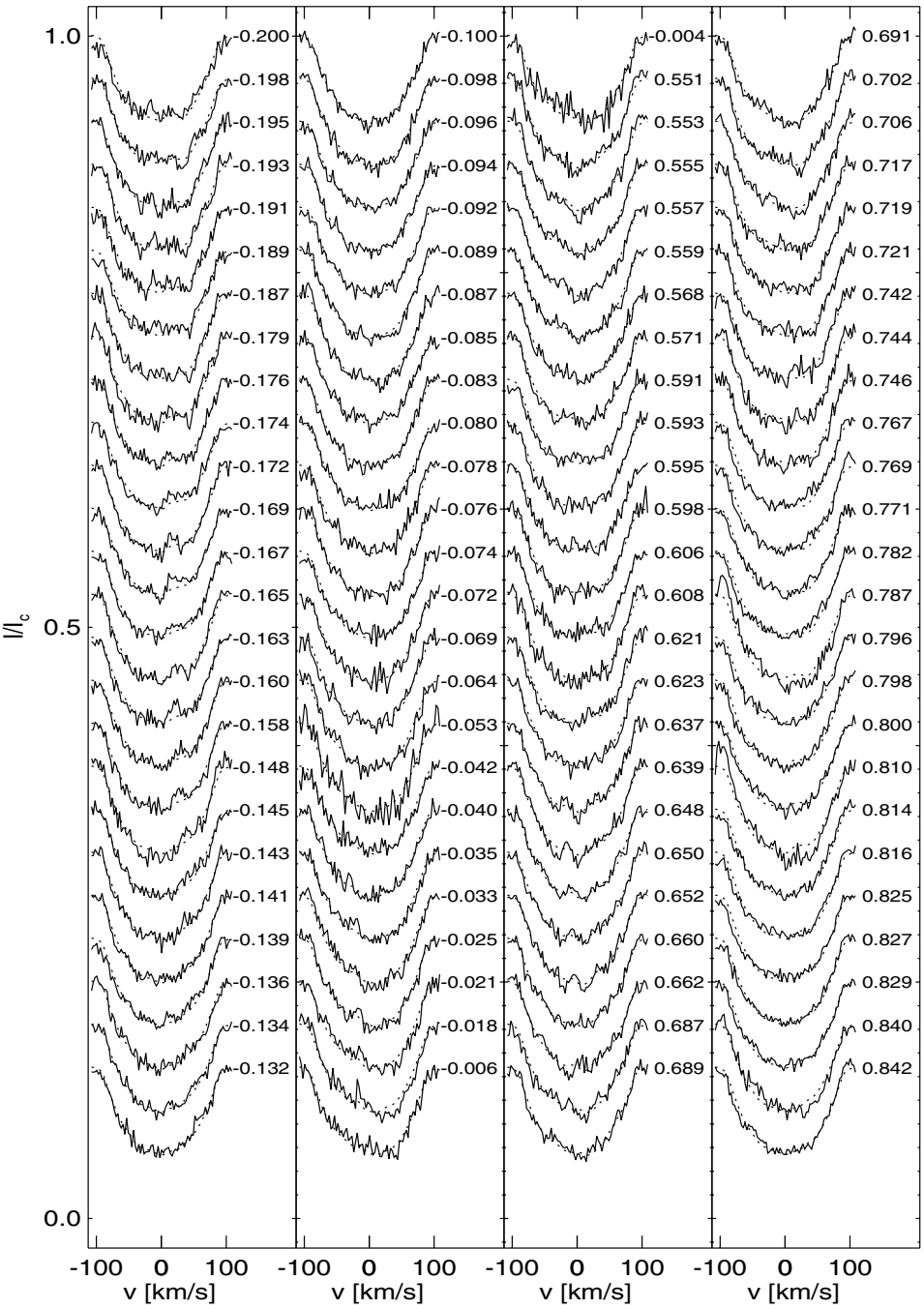

Figure 2. Maximum entropy fits (dashed line) to the LSD profiles (solid line) for 1988 December 16 and 19, observed at the AAT. The rotational phases are indicated to the right-hand side of each profile.

the fragmented polar cap. However, this could result from the low S/N of the data set.

The maximum entropy fits and the reconstructed surface brightness image for 1992 January are shown in Figs 5, 6 and 7. The image is comparable with previous images of this data set processed without LSD Collier Cameron & Unruh (1994) using the Ca I 643.9 nm and Ca 671.8 nm photospheric lines. It is not possible to compare exact features due to the S/N difference, but to a first approximation the two images contain similar spot features at mid to low latitudes. Examples of such features are at phase 0.65, the gap in low- to mid-latitude features at phase 0.35, and the spot features at phase 0.5. Collier Cameron & Unruh (1994) also reconstructed a surface brightness image using the photospheric line Fe I 666.3 nm. However, the reconstructed spot features and groupings are less similar to the image shown in Fig. 7, which is likely to result from the different excitations of the two lines. At high to polar latitudes the images reconstructed in this analysis show a strong and uniform polar cap whereas the images of Collier Cameron & Unruh (1994) show weak and fragmented spot structures. It should be noted that the default value of spot coverage is 0.5 in the work of Collier Cameron & Unruh (1994), while in this analysis we set the value to be 0.999. A surface image has also been reconstructed by Järvinen et al. (2005)

Downloaded from https://academic.oup.com/mnras/article/375/2/567/1442930 by guest on 15 December 2020

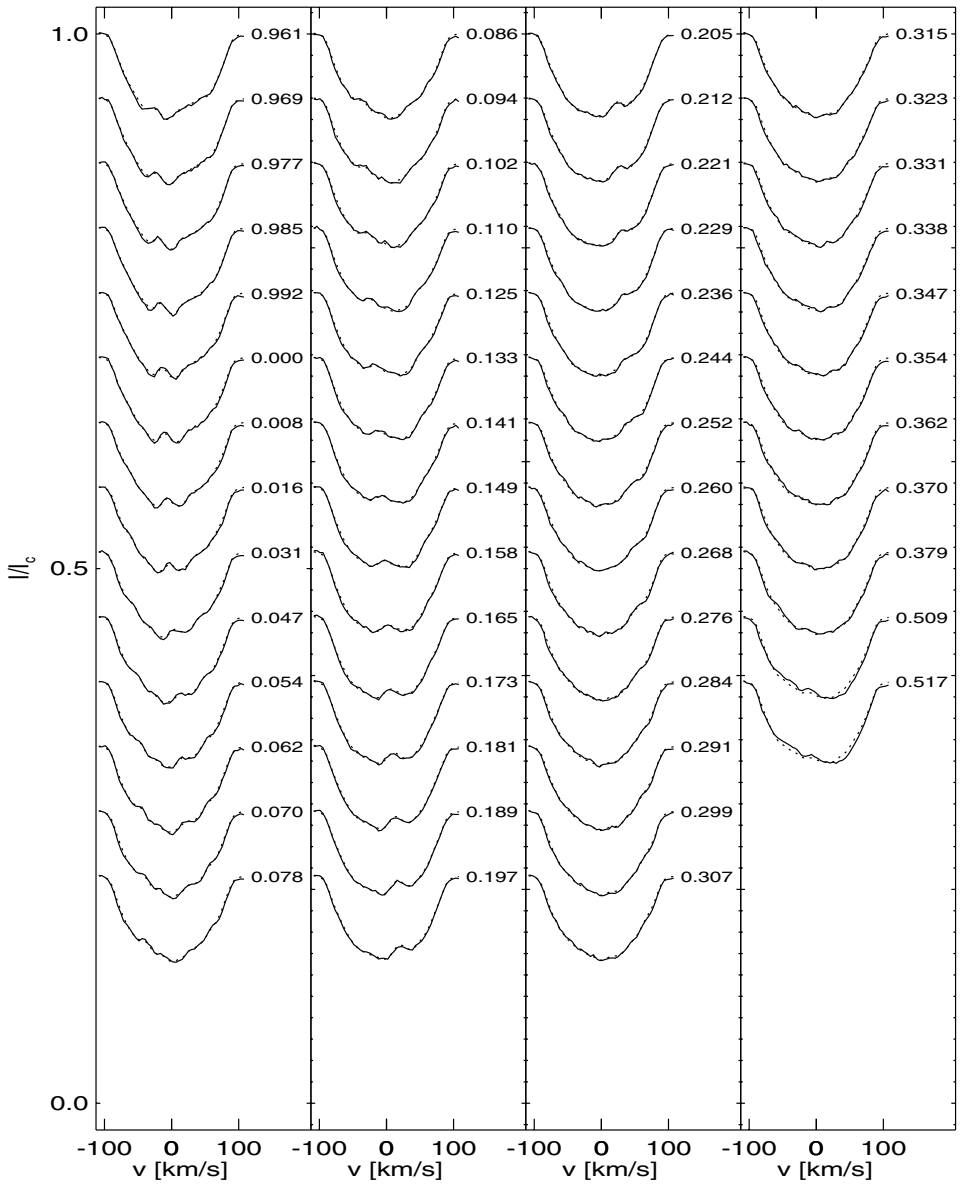

Figure 3. Maximum entropy fits (dashed line) to the LSD profiles (solid line) for 1988 December 21, observed at ESO. The rotational phases are indicated to the right-hand side of each profile.

using photometric data for the epoch 1991.96, which shows a primary spot at phase 0.7 and a weaker secondary spot at phase 1.097. While Fig. 7 shows that there is a fragmented spot structure at phases 0.6–0.8, there is no evidence for a second grouping of spots at phase 1.097.

For the single night of observations in 1992 December the reconstructed surface brightness image (shown in Fig. 8 with fits shown in Fig. 9) is broadly in agreement with that previously reconstructed by Collier Cameron (1995) using Ca I 643.9 nm, Fe I 666.3 nm and Ca I 671.8 nm. Both images show an off-centre polar cap though the spot structure is less fragmented, and the lower latitude features are more clearly resolved in the surface brightness images reconstructed in this analysis. Examples of common features include spots at phases 0.15, 0.28 and 0.45, and a large unspotted area at phase 0.35. For epoch 1992.96 the photometric image reconstruction of Järvinen et al. (2005) shows a primary spot at phase 0.931, and a secondary spot at phase 1.325. Due to missing phase coverage it is not possible to verify the positioning of the primary spot from our Doppler images, but we show that there are no significant spot features present at phase 1.325.

The maximum entropy fits and the reconstructed surface brightness image for 1993 November are shown in Figs 10, 11 and 12. These images were previously reconstructed using the combined lines of Ca I 643.9 nm, Fe I 666.3 nm and Ca I 671.8 nm by Unruh, Collier Cameron & Cutispoto (1995). The images reconstructed in this work have more intermediate and low-latitude spot features. However, there are comparable spot features at phases 0.38–0.55, 0.62, 0.8 and a similar spot grouping at phase 0, though as indicated by the tick marks above the plot, there is no phase coverage in this region. Similar to the comparisons of the 1992 data sets, at high and polar latitudes the spot structure is weaker and more fragmented in the images reconstructed by Unruh et al. (1995). The surface image

Downloaded from https://academic.oup.com/mnras/article/375/2/567/1442930 by guest on 15 December 2020

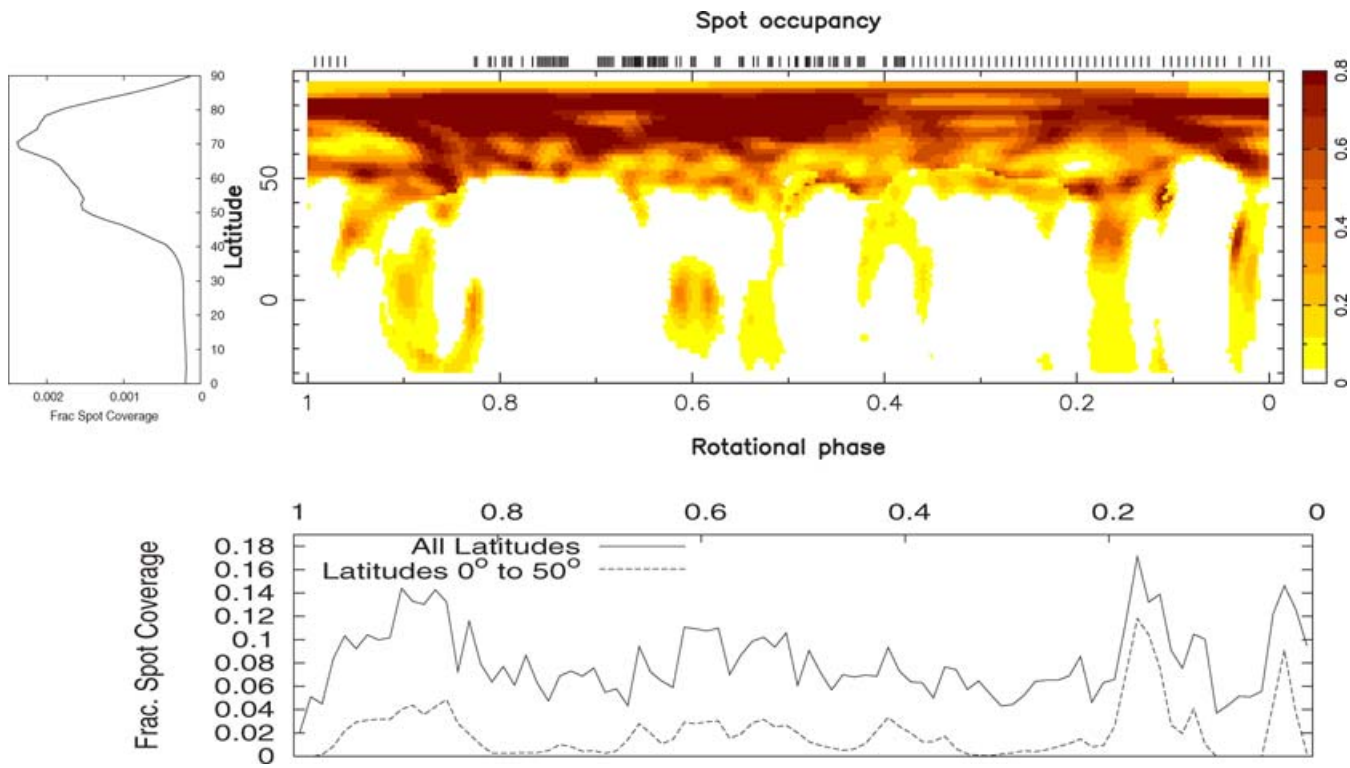

Figure 4. Maximum entropy surface brightness distribution for 1988 December (epoch 1988.96), where the vertical tics at the top of the plot indicate the phase coverage. The plot to the left-hand side shows the fractional spot coverage per latitude bin integrated over longitude, while the plot below shows the fractional spot coverage per rotational phase bin, integrated over latitude.

of Järvinen et al. (2005) at epoch 1993.89 shows a primary spot at phase 1.542 and a secondary spot at phase 1.097. At phase 1.097 in Fig. 12 there is a large grouping of spots, while at phase 1.542 there is a weak spot feature that is insignificant in strength compared to other reconstructed spots at phases 0.38, 0.49 and 0.62.

The maximum entropy fits and the reconstructed surface brightness image for 1994 November are shown in Figs 13, 14 and 15. LSD has previously been applied to the 1994 CTIO data by Collier Cameron et al. (1999). However, in our image reconstructions the polar cap is stronger and less fragmented and at mid to low latitudes the spot features are more resolved. Examples of similar spot features include those at phases 0.1–0.18, 0.25–0.35 and 0.45–0.55. For epoch 1994.87 the surface image of Järvinen et al. (2005) shows a primary spot at phase 1.514, and a secondary spot at phase 1.097. While there is a spot feature at phase 1.514, it is significantly weaker than its neighbouring features, and the spot feature at phase 0.3 in Fig. 15. We have reconstructed a weak spot feature at the phase 1.097, but there are other stronger spots close by at phase 0.3.

At certain phases of the LSD profiles, it is possible to distinguish a shallow absorption feature migrating through the line profile, which is not reproduced in the model maximum entropy profiles. Examples of such features are shown in part II of the 1993 November data set (Fig. 11) at phases 0.565–0.815. We attribute these absorption features as being small regions on the stellar surface that are brighter than the surrounding photosphere in contrast to cooler regions that produce emission features in the line profiles. As the imaging code is designed only to reconstruct cool features on the stellar surface, it is not possible to reconstruct these bright features. The presence of these bright features does not interfere with the reliable reconstruction of cool spots.

5 SURFACE DIFFERENTIAL ROTATION

We used the sheared-image method of Donati et al. (2000) to measure the differential rotation of AB Dor. AB Dor is an ideal candidate to measure differential rotation as its short rotation period (0.514 79-d or 12.2053 rad d^{-1}) means that it is possible to observe up to two-thirds of the stellar surface in one night and to get the necessary overlapping phase coverage within a few days.

The image reconstruction process also incorporates a model of the stellar surface whose rotation rate Ω depends on latitude according to the simplified solar-like differential rotation law:

$$\Omega(\theta) = \Omega_{\rm eq} - \delta\Omega \cos^2\theta, \tag{1}$$

where $\Omega(\theta)$ is the rotation rate at colatitude θ, $\Omega_{\rm eq}$ is the equatorial rotation rate and $\delta\Omega$ is the difference between polar and equatorial rotation rates. We performed a large set of image reconstructions, using a 2D grid of values for the parameters $\Omega_{\rm eq}, \delta\Omega$. For each set of model parameters, the image reconstruction was driven until it reached a fixed value of spot filling factor. The χ^2 values of the resulting images form a 'landscape' on this grid. The best fitting model will corresponds to the minimum in the χ^2 landscape, as models with the wrong shear will give poor fits to the data (Petit, Donati & Collier Cameron 2002).

The optimally fitting differential rotation parameters and their errors are determined by fitting the reduced χ^2 landscape grids with a bi-dimensional paraboloid with linear and quadratic terms given by

$$a\Omega_{\rm eq}^2 + b\Omega_{\rm eq}\,{\rm d}\Omega + c\,{\rm d}\Omega^2 + {\rm d}\Omega_{\rm eq} + e\,{\rm d}\Omega. \tag{2}$$

The five coefficients are then used to solve for $\Omega_{\rm eq}$ and $d\Omega$, and their errors. As discussed by Donati et al. (2003b), the errors are

Downloaded from https://academic.oup.com/mnras/article/375/2/567/1442930 by guest on 15 December 2020

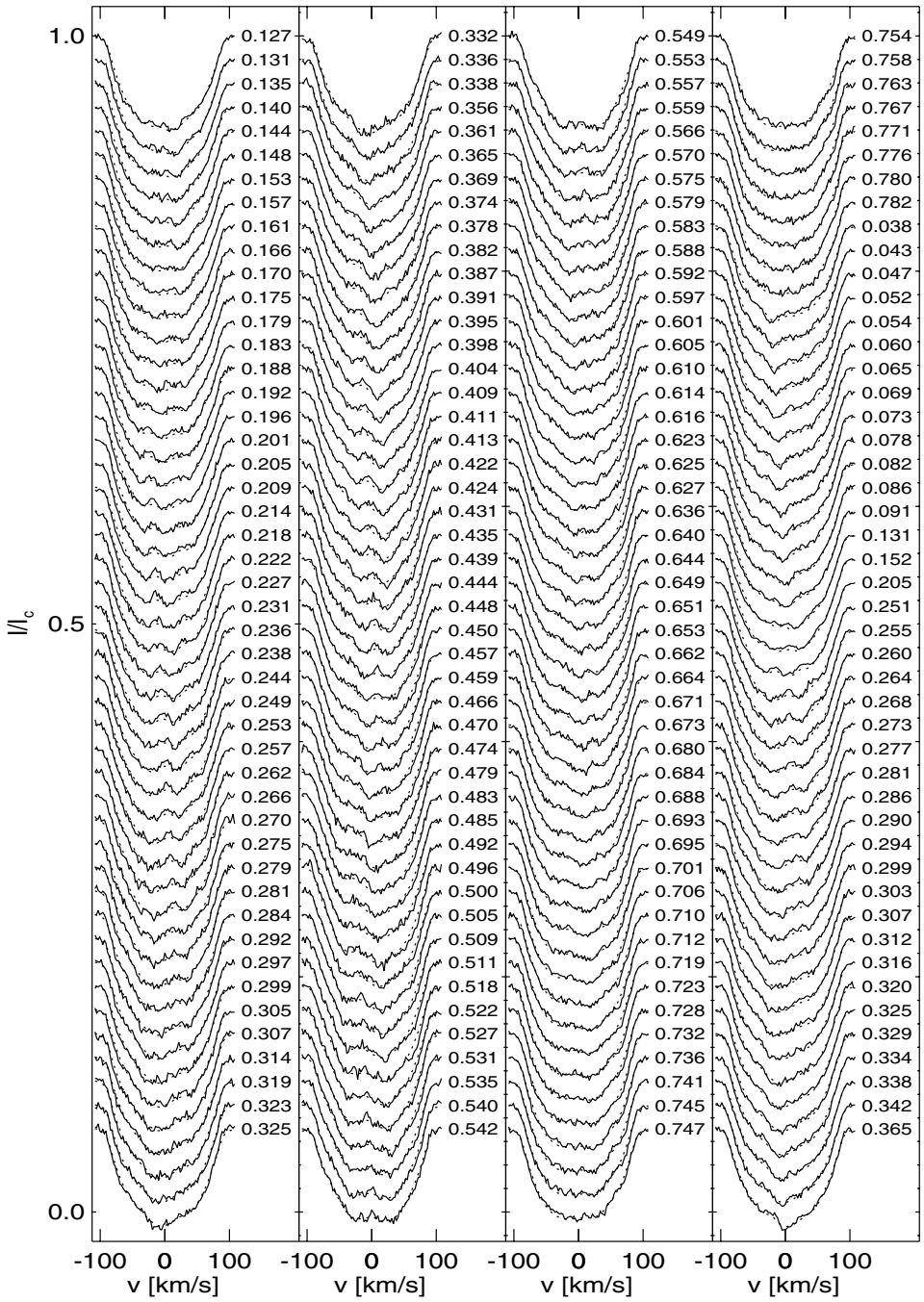

Figure 5. Maximum entropy fits (dashed line) to the LSD profiles (solid line) for 1992 January 18–20, part I. The rotational phases are indicated to the right-hand side of each profile.

determined by computing the curvature radii of the χ^2 paraboloid at its minimum and the correlation coefficient parameter between the two differential rotation parameters.

5.1 Results

For each epoch that comprises more than one night, we converged the imaging code to the fixed spot filling factors obtained when reconstructing the surface brightness images and computed a grid of Ω and d Ω models. The resulting χ^2 landscape is shown in Fig. 16 for epoch 1992.05 and fitting the paraboloid (equation 2) to the data resulted in the values shown in Table 4. The results for epoch 1988.96 resulted in a map without any minimum, which is attributed to the poor quality of this data set. The temporal evolution of differential rotation over the epochs of this analysis is plotted in Fig. 17. This plot clearly shows that the magnitude of temporal evolution is greater than the error bars of the differential rotation measurements, with the most noticeable change in dΩ of 11.0 m rad d^{-1} being between epochs 1992.05 and 1993.89.

Downloaded from https://academic.oup.com/mnras/article/375/2/567/1442930 by guest on 15 December 2020

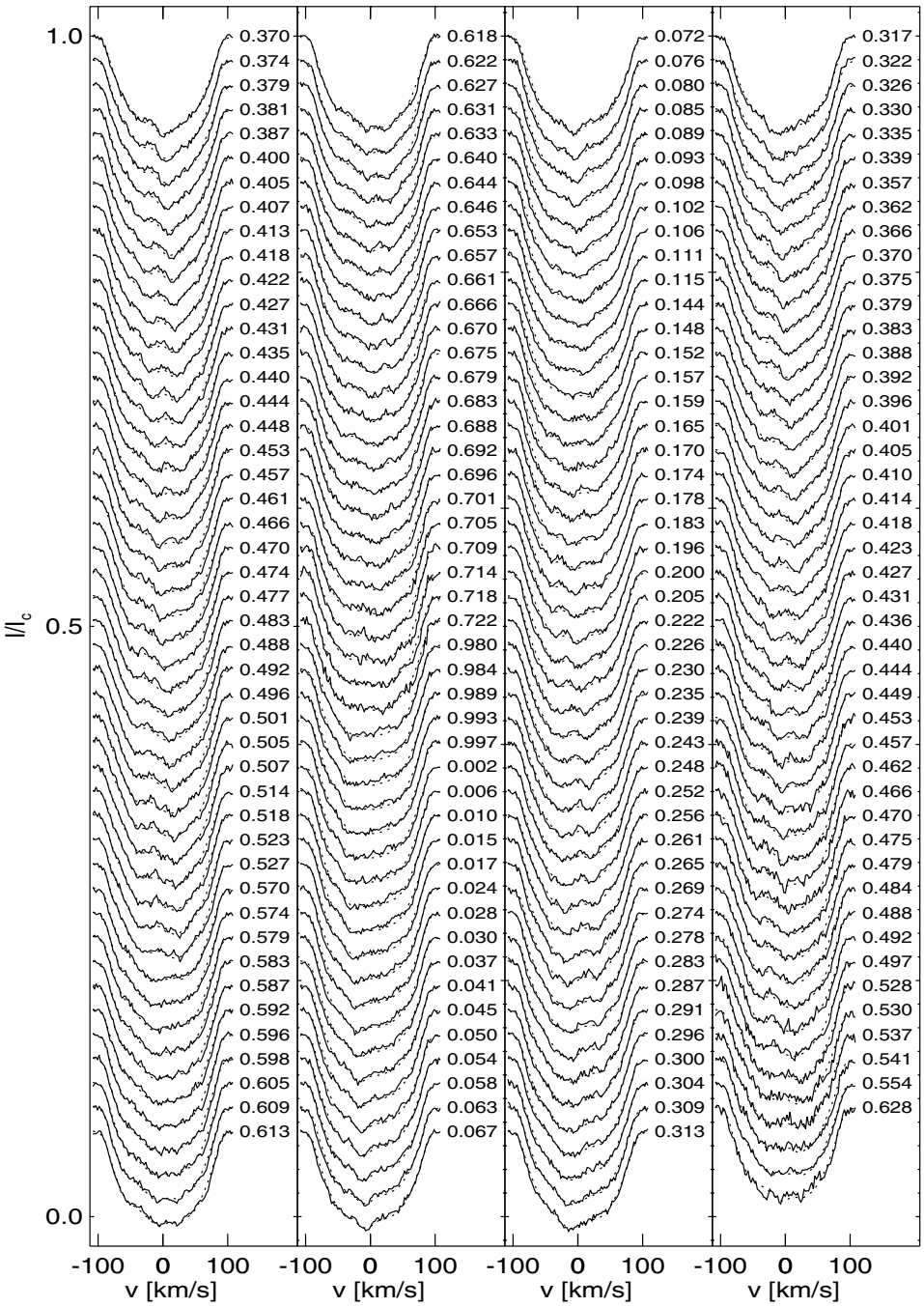

Figure 6. Maximum entropy fits (dashed line) to the LSD profiles (solid line) for 1992 January 18–20, part II. The rotational phases are indicated to the right-hand side of each profile.

6 DISCUSSION

6.1 Star-spot distributions

AB Dor is one of the most extensively Doppler imaged stars. In this analysis we have extended the work of Donati & Collier Cameron (1997), Donati et al. (1999) and Donati et al. (2003a) to include epochs 1988.96, 1992.05, 1992.95, 1993.89 and 1994.87 to have a complete data set that has been processed using the same processing methods. One outstanding feature present at all epochs is a long-lived polar cap that is slightly fragmented at epoch 1988.96 and weaker at epoch 1992.95. Direct evidence for the presence of a polar cap has been shown by Jeffers et al. (2005) and Jeffers et al. (2006) using data from the *Hubble Space Telescope* of the RS CVn binary SV Cam. The reconstructed surface images of this analysis also show many small mid- to low-latitude spots and a spot coverage that ranges from 6.25 per cent at epoch 1992.95 to 9.2 per cent at epoch 1994.87. These values bear no resemblance to the results of long-term photometric measurements, which show a brightness minimum in 1988 (Amado et al. 2001). The difference between the two results can be accounted for by the presence of chromospheric emission, which for young stars such as AB Dor, shows an

Downloaded from https://academic.oup.com/mnras/article/375/2/567/1442930 by guest on 15 December 2020

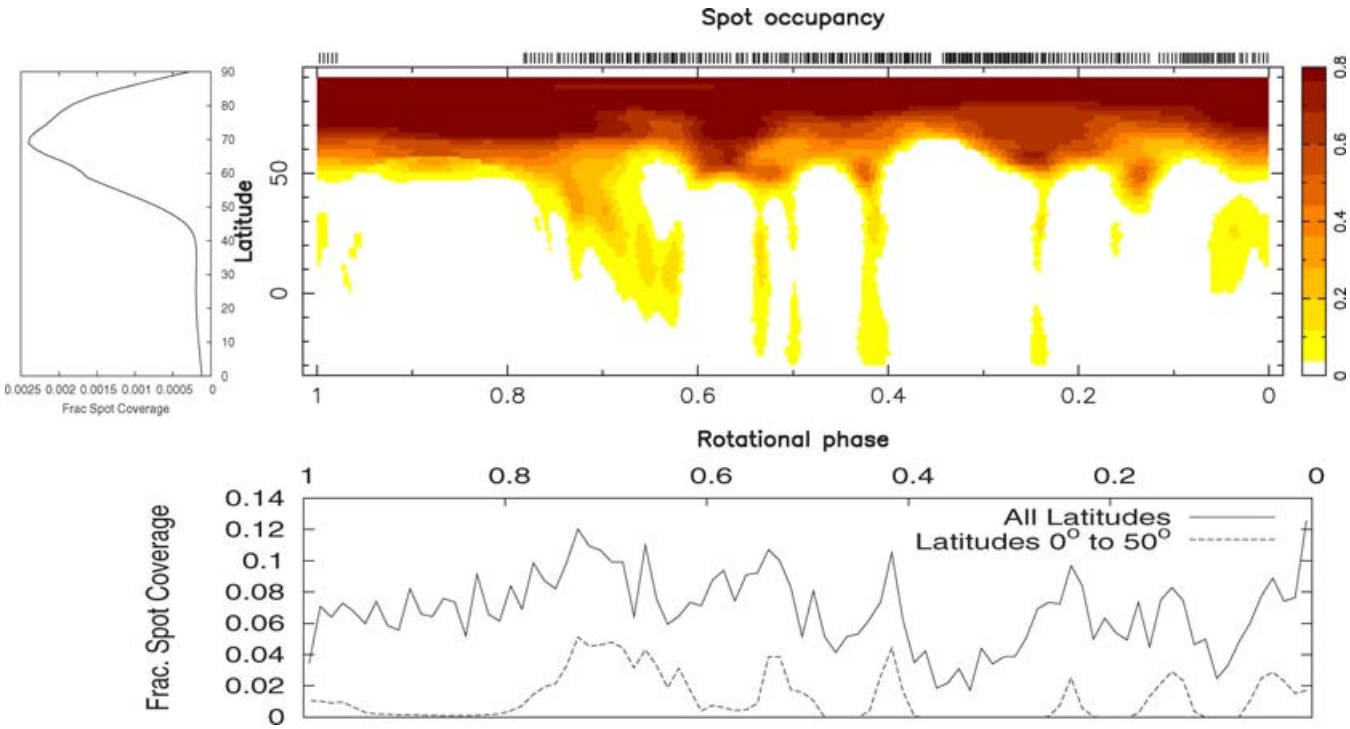

Figure 7. Maximum entropy surface brightness distribution for 1992 January (epoch 1992.05), where the vertical tics at the top of the plot indicate the phase coverage. The plot to the left-hand side shows the fractional spot coverage per latitude bin integrated over longitude, while the plot below shows the fractional spot coverage per rotational phase bin, integrated over latitude.

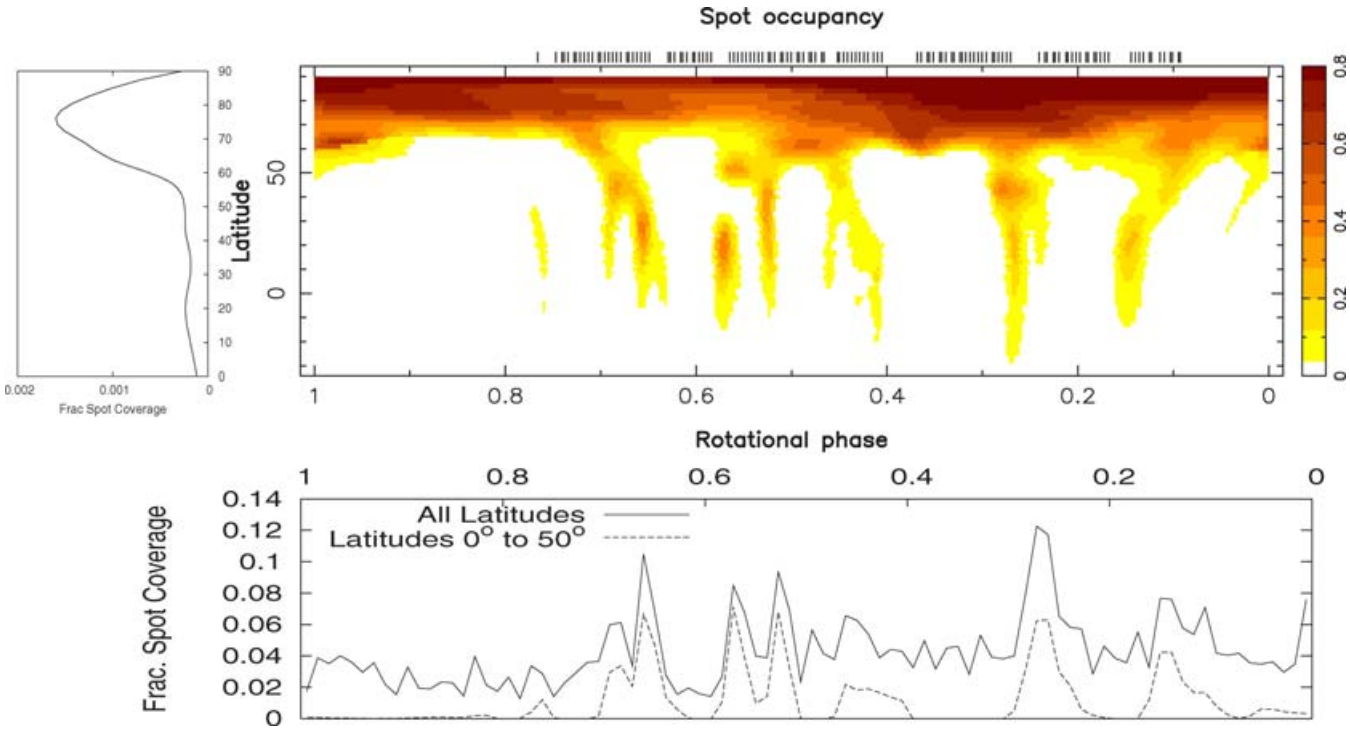

Figure 8. Maximum entropy surface brightness distribution for 1992 December (epoch 1992.95), where the vertical tics at the top of the plot indicate the phase coverage. The plot to the left-hand side shows the fractional spot coverage per latitude bin integrated over longitude, while the plot below shows the fractional spot coverage per rotational phase bin, integrated over latitude.

Downloaded from https://academic.oup.com/mnras/article/375/2/567/1442930 by guest on 15 December 2020

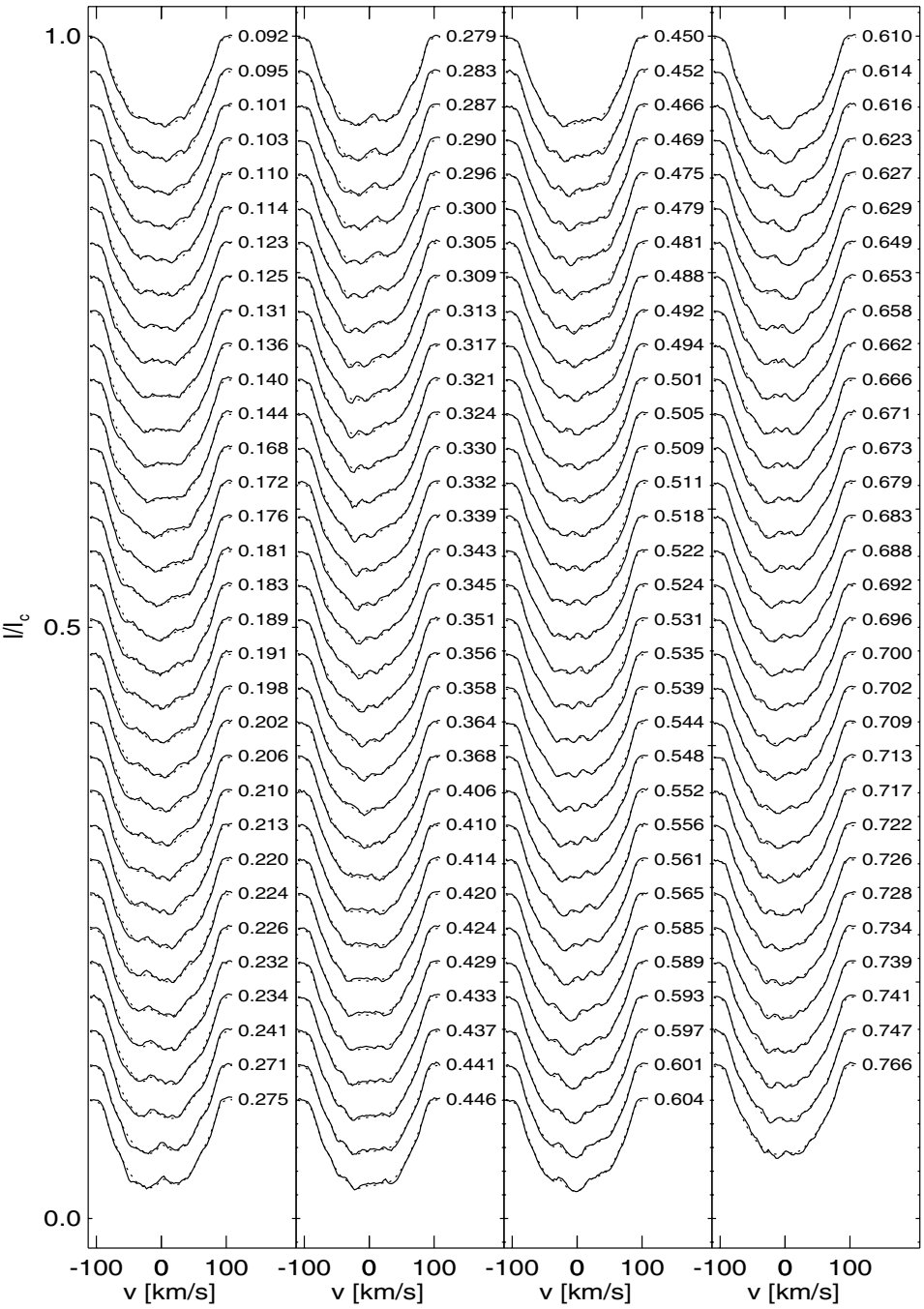

Figure 9. Maximum entropy fits (dashed line) to the LSD profiles (solid line) for 1992 December 14. The rotational phases are indicated to the right-hand side of each profile.

anticorrelation with the star's photometric variations (Radick et al. 1998).

For 1988.96 the reconstructed weak and fragmented polar cap is not conclusive due to the poor S/N of the data. However, there is additional evidence from the results of Kürster, Schmitt & Cutispoto (1994) that AB Dor did not posses a polar cap in 1989. This could show that these large polar caps could disappear periodically. If such behaviour is cyclic then this could be related to a change in the dynamo nature of the star. The weaker polar cap for epoch 1992.95 probably results from the lower overall spot coverage at this epoch.

The long-term stability of high, mid and low latitudes is shown to vary on a time-scale that is shorter than the temporal spacing of our observations. The evolution of small-scale magnetic features has been shown by Barnes et al. (2001) to be on a time-scale of less than one month for the active G2 dwarf He 699. The fractional spot coverage per latitude bin for each epoch of this analysis is shown in Fig. 18. The relative fractional spot coverage for low-latitude features (between 0° and 50°) is 24 per cent for 1988.96, 17 per cent for 1992.05, 26 per cent for 1992.95, 30 per cent for 1993.89 and 19 per cent for 1994.87. The yearly distributions as shown in Fig. 18 show that the peak does not become broader with time indicating

Downloaded from https://academic.oup.com/mnras/article/375/2/567/1442930 by guest on 15 December 2020

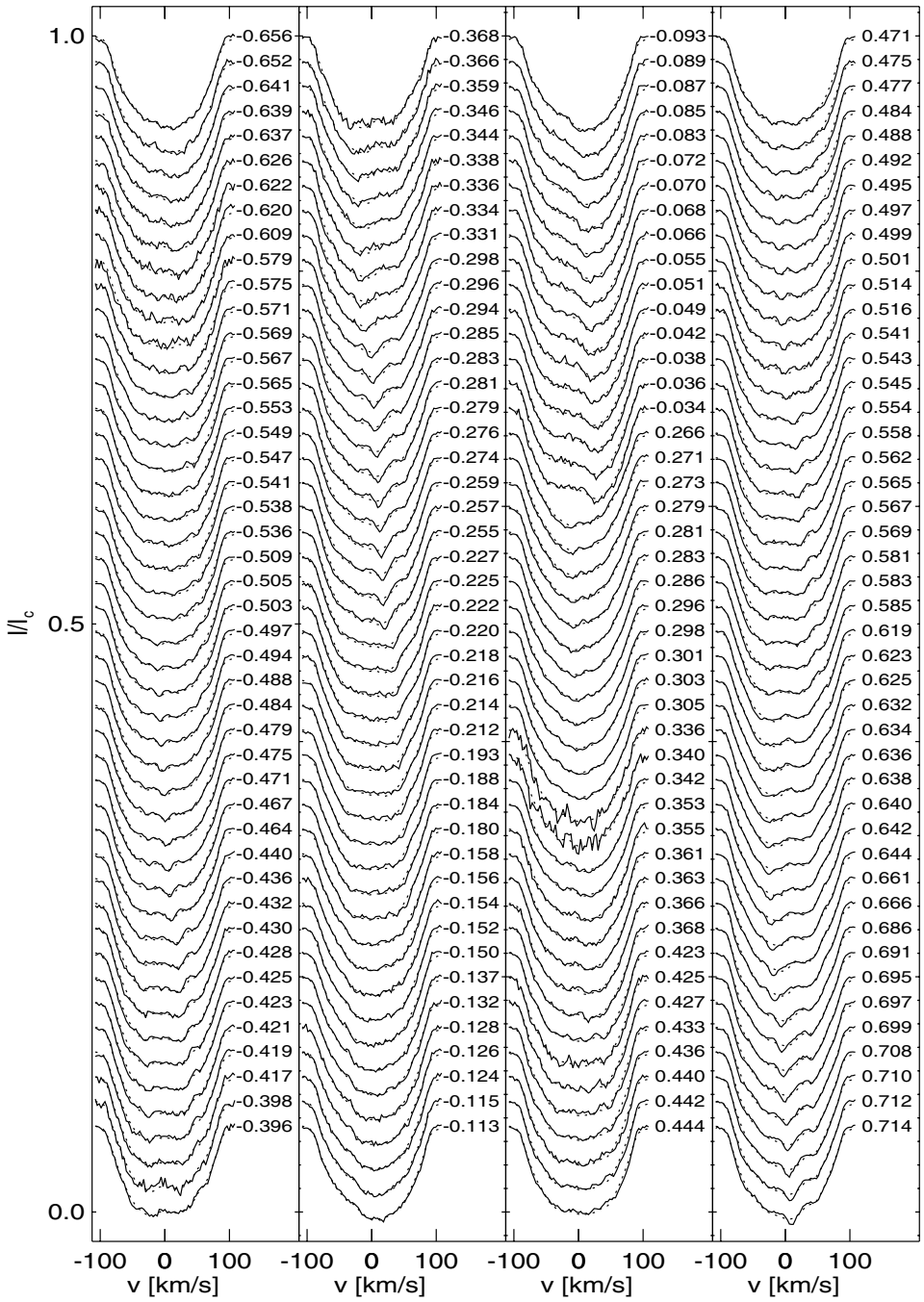

Figure 10. Maximum entropy fits (dashed line) to the LSD profiles (solid line) for 1993 November 23–25, part I. The rotational phases are indicated to the right-hand side of each profile.

that there is no apparent migration of high-latitude spots towards the equator. However, this plot does show a global evolution of the spot distribution with possibly the polar spot becoming weaker with time and more spots forming at lower latitudes (compare plots for 1993.89 and 1998.96/1992.05). In contrast to these results, Järvinen et al. (2005) show, from photometric data of AB Dor at similar epochs, that the mean spot latitude of 47°–51° for 1992.05 and 45° for 1993.89 is significantly lower than the values of this analysis.

The integrated brightness distributions are plotted as a function of longitude for each surface brightness image, as shown in the lower panel of Figs 4, 7, 8, 12 and 15. These distributions show a variation of spot coverage with longitude, and regions of concentrated spot coverage that could be indicative of regions of enhanced magnetic activity or 'active longitudes'. Active longitudes are shown to be present on AB Dor by Järvinen et al. (2005), where they reconstruct surface images comprising a primary and secondary spots from photometric data. The effect of high spot coverage can in, certain cases, result in spurious 'active longitudes' though these are always located at the quadrature points (Jeffers 2005).

As previously discussed we show that the Doppler images reconstructed here are in broad agreement with the location of the primary

Downloaded from https://academic.oup.com/mnras/article/375/2/567/1442930 by guest on 15 December 2020

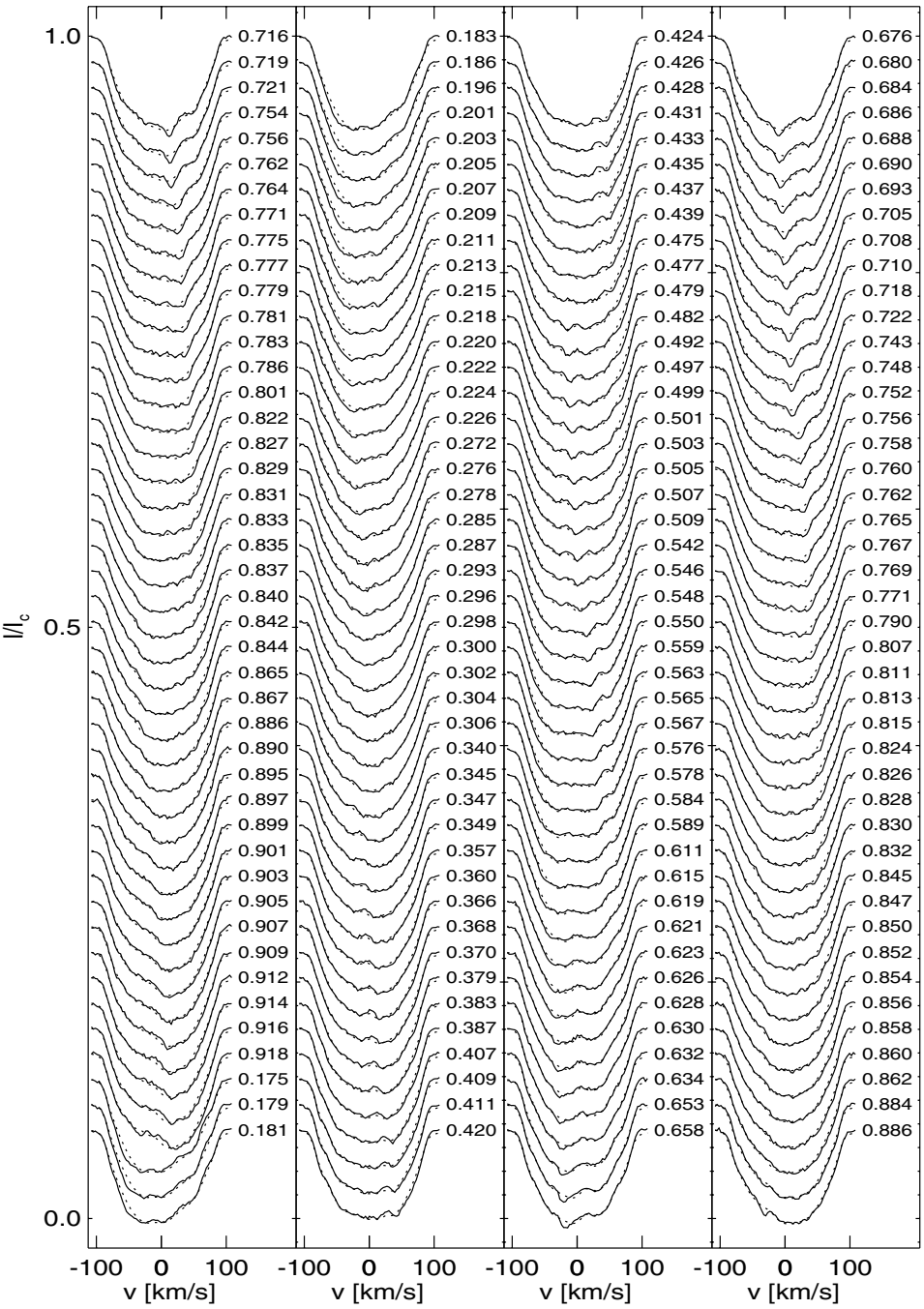

Figure 11. Maximum entropy fits (dashed line) to the LSD profiles (solid line) for 1993 November 23–25, part II. The rotational phases are indicated to the right-hand side of each profile.

spot of Järvinen et al. (2005), but not with the existence or location of a secondary spot. The difference between the results of this analysis and those of Järvinen et al. (2005) is not a result of inaccurate photometric data, but due to that it is not possible to correlate phases of maximum and minimum photometric brightness with regions of the highest and lowest density of low-latitude features. This is because the shape of the light curve can also be strongly influenced by the presence of high-latitude features and an off-centred polar cap. The effect of including high-latitude spot features and polar cap is shown in the plots of the fractional spot coverage as a function of longitude (lower plot of Figs 4, 7, 8, 12 and 15) where plots are shown for spot features integrated over all latitudes and between 0° and 50°. For epochs 1988.96 and 1993.89 there is little difference in the general shape of the two integrated spot coverage distributions. However, for epoch 1992.05 there are notable differences at phases 0.27–0.4 and 0.8–0.95: in particular the degree of fractional spottedness of the plot integrated over all latitudes (approximately 0.02 for phases 0.27–0.4 and 0.06 for phases 0.8–0.95), both show the same level of spottedness when integrated only between latitudes 0° and 50° when this is clearly not the case when integrated between

Downloaded from https://academic.oup.com/mnras/article/375/2/567/1442930 by guest on 15 December 2020

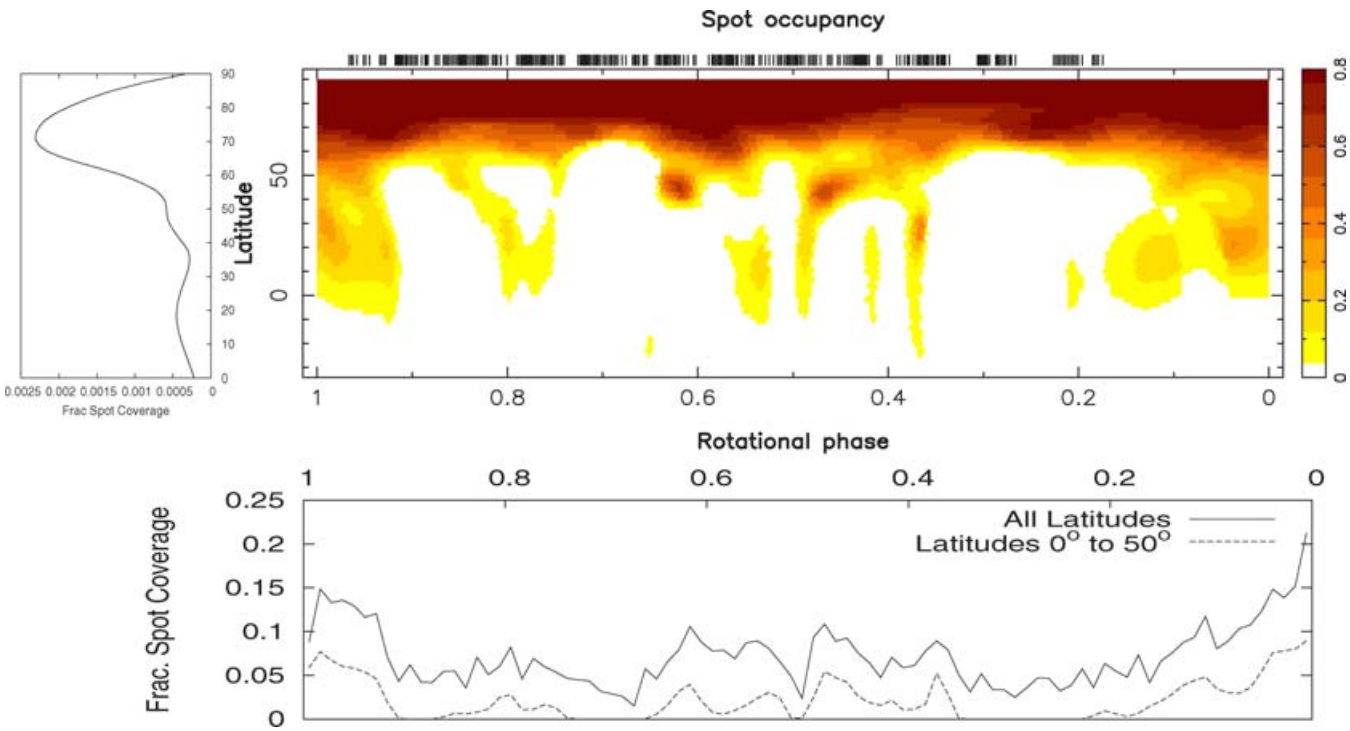

Figure 12. Maximum entropy surface brightness distribution for 1993 November (epoch 1993.89), where the vertical tics at the top of the plot indicate the phase coverage. The plot to the left-hand side shows the fractional spot coverage per latitude bin integrated over longitude, while the plot below shows the fractional spot coverage per rotational phase bin, integrated over latitude.

0° and 90°. The same traits can be seen in the fractional spot distributions of epochs 1992.95 and 1994.87. Similar conclusions have also been reached by Donati et al. (2003a) and Vogt et al. (1999). Additionally, our image reconstructions also do not show evidence for the migration of both primary and secondary spots at a constant separation or 'flip-flops' as shown in the work of Järvinen et al. (2005).

6.2 Differential rotation

Surface differential rotation was measured for epochs with sufficient overlapping phase coverage, for example, 1992.05, 1993.89 and 1994.87. In a complimentary paper, Donati, Collier Cameron & Petit (2003b) measure differential rotation on AB Dor for epochs after 1995 using the same method of this analysis. The resulting values of $d\Omega$ and Ω_{eq} for all epochs are shown in Fig. 17. This plot clearly shows that the results of this paper are generally higher than previous results with 1994.87 having the highest differential rotation ever measured on AB Dor. The smaller size of the error ellipses shown in Fig. 17 for epochs after 1994.87 are because the data set was taken over a longer time period enabling a more accurate differential rotation measurement to be made. The results so far, from 1992.05 to 2001.99, show no evidence for any cyclic behaviour.

Another single dwarf with a similar spectral type to AB Dor and for which there have been multiple measurements of differential rotation is the K2V dwarf LQ Hya. Only two measurements, a year apart, have been made with more than a magnitude of variation in $\Delta\Omega$ ranging from 0.1942 rad d^{-1} to 0.014 40 rad d^{-1}. The large difference in measurements could result from the rotational period of LQ Hya being about three times that of AB Dor and hence the spatial resolution at the stellar surface is much less than that on AB Dor. This could result in the measurement of differential rotation being influenced by the short-term evolution of unresolved spots.

The temporal evolution of differential rotation of AB Dor has also been determined by Collier Cameron & Donati (2002), using a method that tracks individual star-spots in the dynamic spectrum, for the same epochs of this analysis. The results of this method show a stronger differential rotation measurement for all epochs; 1992.05 ($\Omega_{eq} = 12.2514 \pm 0.0029$ rad d^{-1} and $d\Omega = 91.05 \pm 13.19$ m rad d^{-1}), 1993.97 ($\Omega_{eq} = 12.2502 \pm 0.0024$ rad d^{-1} and $d\Omega = 88.49 \pm 7.47$ m rad d^{-1}) and 1994.87 ($\Omega_{eq} = 12.2481 \pm 0.0047$ rad d^{-1} and $d\Omega = 66.84 \pm 14.93$ m rad d^{-1}). Donati et al. (2003b) discusses the discrepancy of measurements using the two methods. It is concluded that there are two contributing factors: (i) the value of $v \sin i$ used – the spot-tracking method, which is sensitive to $v \sin i$, uses a value of 89 km s^{-1}, while we use 91 km s^{-1} in this analysis; and (ii) the weighting of individual spots – the sheared imaged method of this analysis places a higher weighting on larger spots, while the spot-tracking method places equal weighting on all spots. However, despite these small-scale differences, the general trend of higher values of differential rotation for the epochs of this analysis are in agreement.

Additionally, Donati et al. (2003b) also measure differential rotation using magnetic features, which give a different result than using cool spots alone. This is interpreted as being evidence that the dynamo is distributed throughout the convective zone and not confined at the base. They also compare their results with models of the differential rotation in the convection zone and show that the internal rotation velocity field is not like that of the Sun, but more like that of rapid rotators where the angular velocity is constant along cylinders aligned with the rotation axis. Donati et al.

Downloaded from https://academic.oup.com/mnras/article/375/2/567/1442930 by guest on 15 December 2020

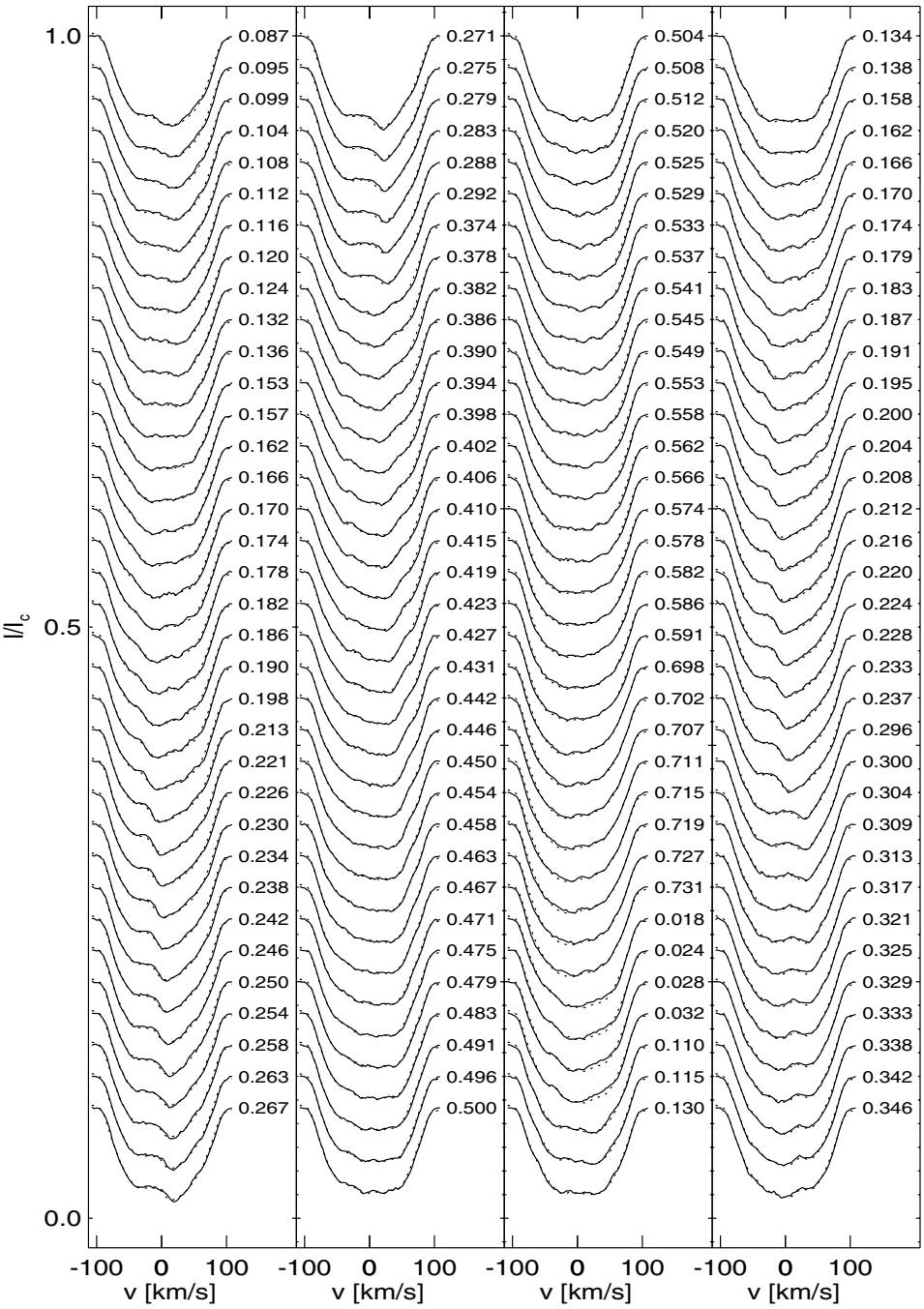

Figure 13. Maximum entropy fits (dashed line) to the LSD profiles (solid line) for 1994 November 15–17, part I. The rotational phases are indicated to the right-hand side of each profile.

(2003b) conclude that changes in differential rotation could result from underlying dynamo processes.

The temporal evolution of differential rotation will also have important consequences for the stellar structure. Large variations will alter the spherical oblateness of the star, such that if AB Dor was in a close binary system it would produce long-term changes in the star's orbital period. This is not applicable to the AB Dor A/C system given their comparatively large (2.3 au) separation. Further support is given to the conjecture of Donati et al. (2003b) by Applegate (1992), Lanza et al. (1998), Lanza & Rodonò (1999) and Lanza (2005), where theoretical interpretations of the orbital period modulation in RS CVns is related to the operation of a hydromagnetic dynamo in the magnetically active star. The model of Applegate (1992) assumes that these periodic modulations are caused by the stellar magnetic cycle converting kinetic energy in the convective zone into large-scale magnetic fields. This is extended by Lanza et al. (1998) and Lanza & Rodonò (1999) to include the effect of magnetic fields on the hydrostatic equilibrium of the magnetically active component. These models have been further extended by Lanza (2005) to include an improved treatment of angular momentum transport

Downloaded from https://academic.oup.com/mnras/article/375/2/567/1442930 by guest on 15 December 2020

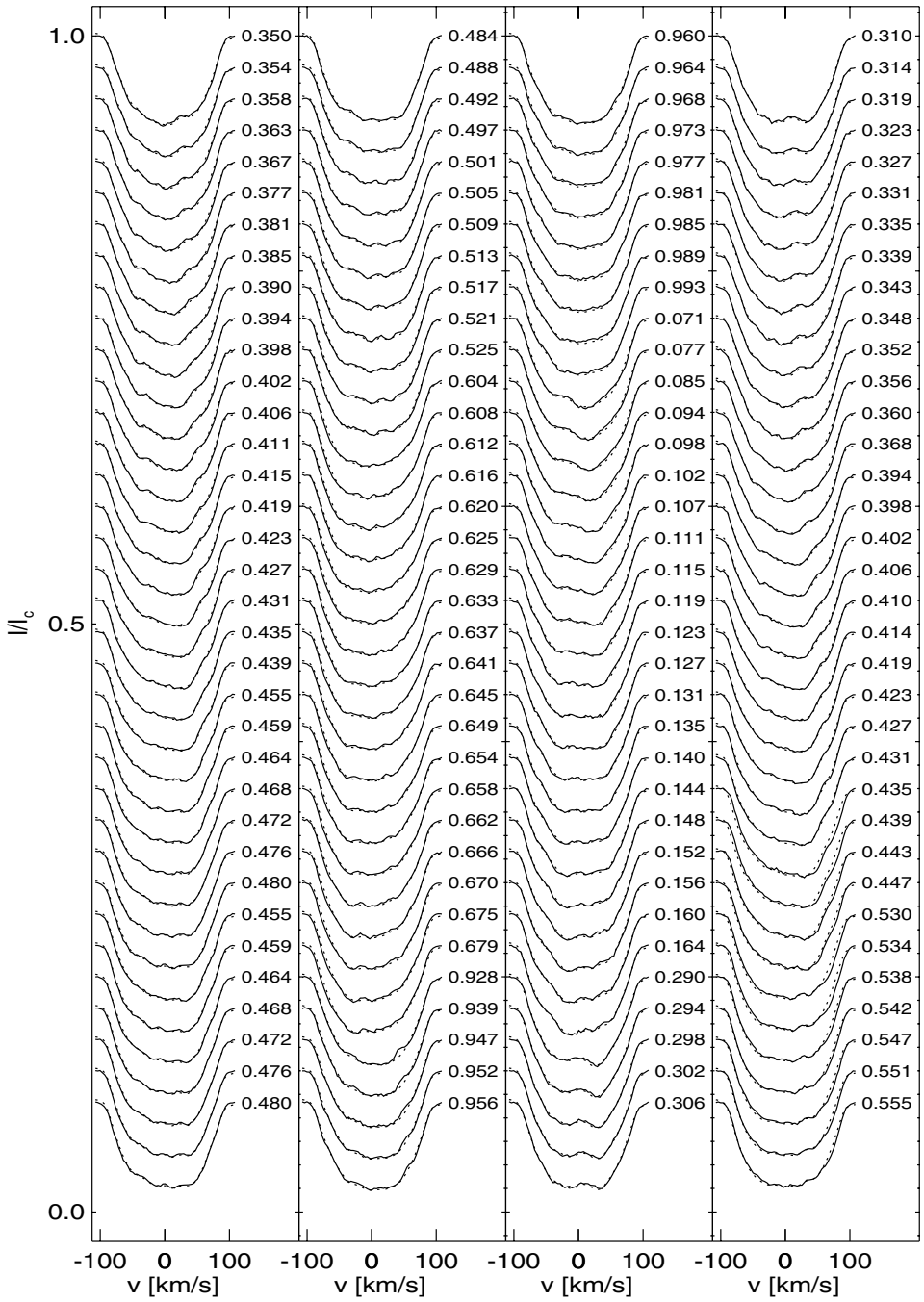

Figure 14. Maximum entropy fits (dashed line) to the LSD profiles (solid line) for 1994 November 15–17, part II. The rotational phases are indicated to the right-hand side of each profile.

in the stellar convective zone, but they conclude that the method of Applegate (1992) is not sufficient to fully explain the mechanisms of orbital migration in close binaries.

7 CONCLUSIONS

In this paper, Doppler images of the magnetically active star AB Dor show that its star-spot coverage is dominated by a long-lived and stable polar cap and variable high- to low-latitude spot coverage. The exception to this is the surface brightness reconstruction of epoch 1988.96 where there is evidence of a weak and fragmented polar cap. There is no cyclic behaviour found in either the latitude distribution of spots or the spot coverage fractions. Our surface brightness reconstructions generally show longitudes where there is a concentration of spots. However, we do not find a second or minor spot concentration which would verify the presence of active longitudes or flip-flop cycles on AB Dor.

We have made the first measurements of differential rotation on AB Dor for epochs 1992.05, 1993.89 and 1994.87. The results show a temporal evolution, with epoch 1994.87 showing the highest value

Downloaded from https://academic.oup.com/mnras/article/375/2/567/1442930 by guest on 15 December 2020

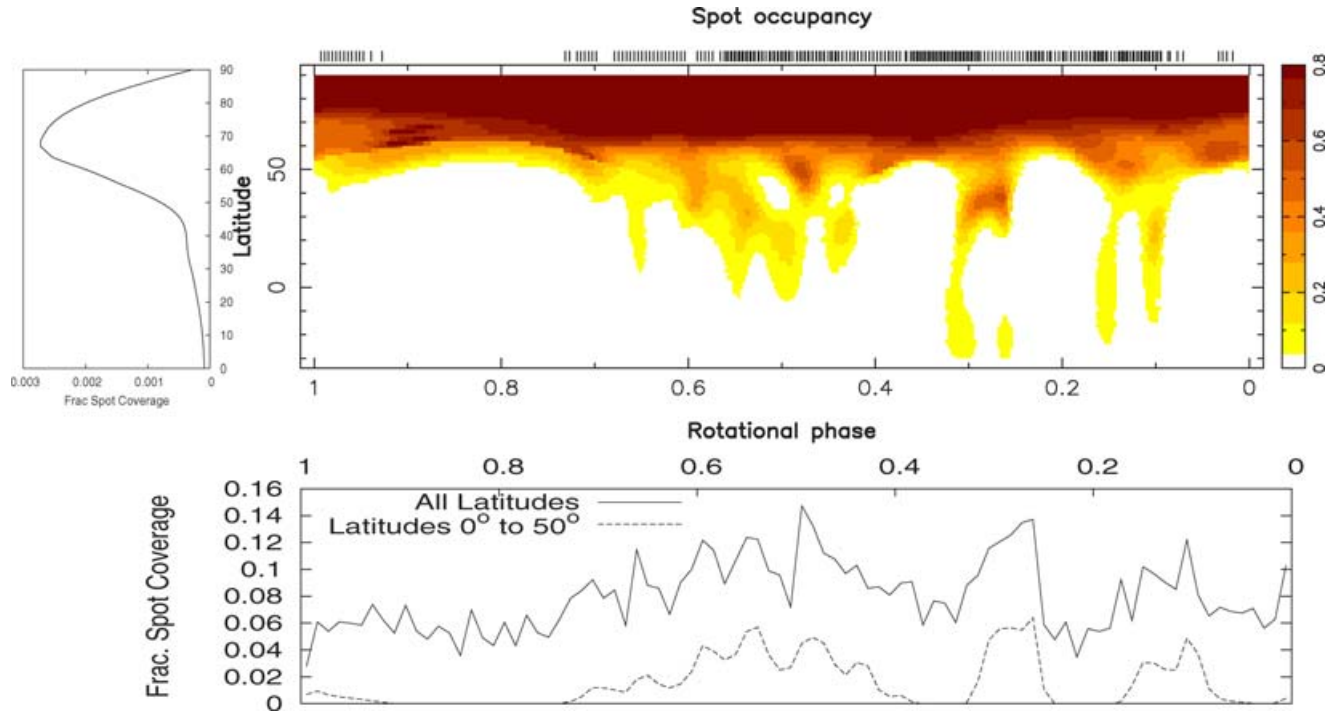

Figure 15. Maximum entropy surface brightness distribution for 1994 November (epoch 1994.87), where the vertical tics at the top of the plot indicate the phase coverage. The plot to the left-hand side shows the fractional spot coverage per latitude bin with integrated over longitude, while the plot below shows the fractional spot coverage per rotational phase bin, integrated over latitude.

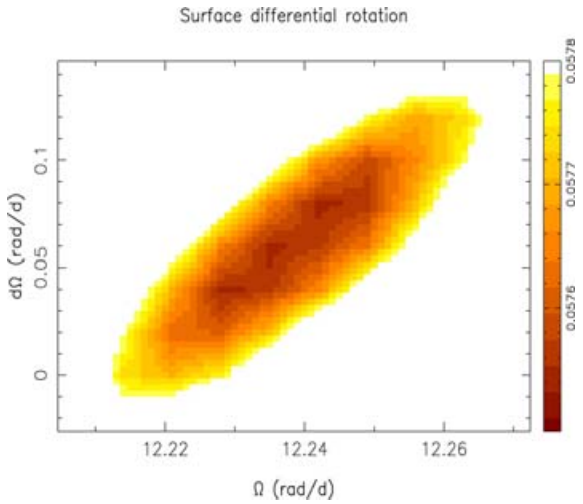

Figure 16. Reduced χ^2 maps showing the differential rotation profile for epoch 1992.05. Only points that are within 1 per cent of the minimum χ^2 are shown. The central black region corresponds to points where the minimum value of differential rotation was obtained, while the outer grey points correspond to the 1.5σ confidence ellipse (taking each parameter separately) on the differential rotation parameter plane.

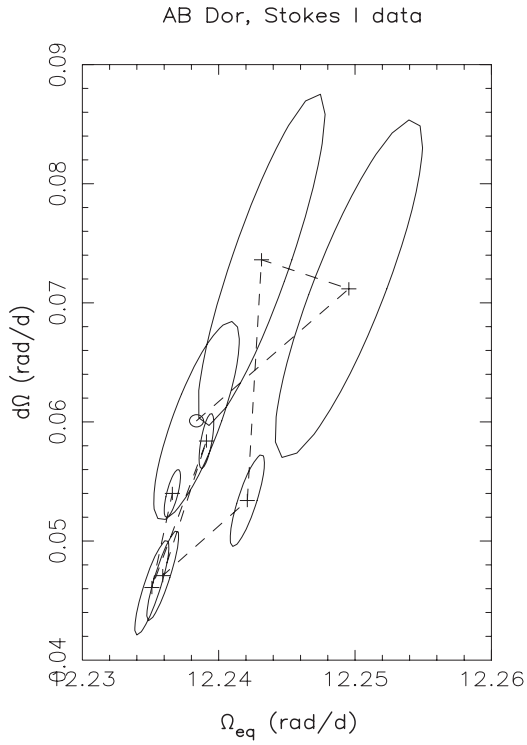

Figure 17. Differential rotation parameters measured for AB Dor as tabulated in Table 4 for epochs 1992.05, 1993.89 and 1994.87 (from this work) and 1995.94, 1996.99, 1999.00, 2000.93, 2001.99 (from Donati et al. 2003b). The central point that is indicated by ○ is for epoch 1992.05 from which a dashed line connects the points in chronological order. The central point is the best-fitting differential rotation measurement. For each differential rotation measurement, the 68 per cent confidence ellipse is also plotted.

of differential rotation ever measured on AB Dor. To a first-order approximation the temporal evolution of differential rotation show the same variation as the results for the same data reconstructed by Collier Cameron & Donati (2002). The results of this work when combined with other previously published papers represents the first long-term analysis of the detailed temporal evolution of differential rotation on magnetically active stars.

Downloaded from https://academic.oup.com/mnras/article/375/2/567/1442930 by guest on 15 December 2020

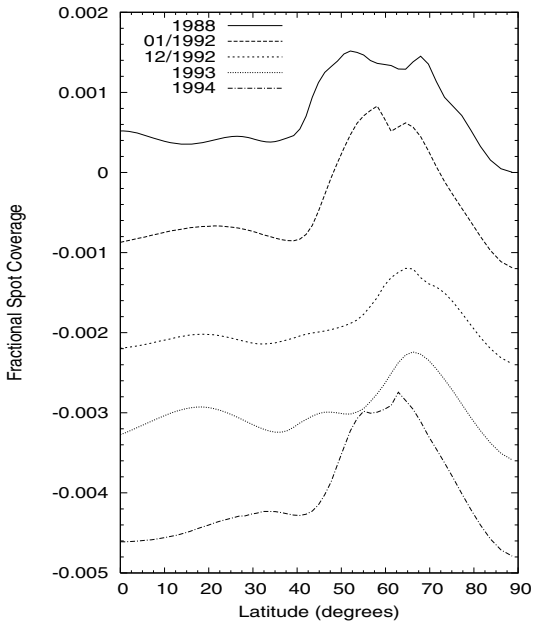

Figure 18. Variation of the fractional spot coverage per latitude bin over the epochs of this analysis.

Table 4. Summary of differential rotation parameters measured for AB Dor at each epoch, where Ω_{eq} is the derived equatorial rotation rate at the 1σ 68 per cent confidence interval, $d\Omega$ is the equator–pole differential rotation rate, column 4 is the inverse slope of the ellipsoid in the Ω_{eq}–Ω plane (equal to $\cos^2\theta_s$, refer Donati et al. 2003b), Ω_s is the rotation rate at colatitude θ_s and n is the total number of data points used in the imaging process.

Epoch	Ω_{eq} (m rad d^{-1})	$d\Omega$ (m rad d^{-1})	$\cos^2\theta_s$	Ω_s (rad d^{-1})	n
1992.05	12 238.3 ± 2.1	60.1 ± 5.5	0.319	12.219	37 761
1993.89	12 249.5 ± 3.5	71.1 ± 9.3	0.338	12.226	26 645
1994.87	12 243.1 ± 3.1	73.6 ± 9.2	0.300	12.221	17 141

ACKNOWLEDGMENTS

This paper is based on observations made using the 3.9-m Anglo-Australian Telescope, the 3.6-m telescope at ESO and the 4-m telescope at CTIO. We thank the referee Steve Saar for suggesting several improvements to the paper. SVJ currently acknowledges support from a personal Marie Curie Intra-European fellowship funded within the 6th European Community Framework Programme. While at St Andrews University SVJ was supported by PPARC and a scholarship from the University of St Andrews, and would like to thank the Scottish International Education Trust for financing a Travel Grant for a collaborative visit to OMP.

REFERENCES

Amado P. J., Cutispoto G., Lanza A. F., Rodonò M., 2001, in García López R. J., Rebolo R., Zapatero M., eds, ASP Conf. Ser. Vol. 223, 11th Cambridge Workshop on Cool Stars, Stellar Systems and the Sun. Astron. Soc. Pac., San Francisco, p. 895
Applegate J. H., 1992, ApJ, 385, 621
Babcock H. W., 1965, Astrophys. Space Sci. Library, 3, 7
Barnes J. R., Collier Cameron A., James D. J., Steeghs D., 2001, MNRAS, 326, 1057
Barnes J. R., Cameron A. C., Donati J.-F., James D. J., Marsden S. C., Petit P., 2005, MNRAS, 357, L1
Brown S. F., Donati J.-F., Rees D. E., Semel M., 1991, A&A, 250, 463
Brun A. S., Toomre J., 2002, ApJ, 570, 865
Bruning D. H., 1981, ApJ, 248, 274
Close L. M. et al., 2005, Nat, 433, 286
Collier Cameron A., 1992, Lecture Notes in Physics, 397, 33
Collier Cameron A., 1995, MNRAS, 275, 534
Collier Cameron A., Unruh Y. C., 1994, MNRAS, 269, 814
Collier Cameron A., Donati J.-F., 2002, MNRAS, 329, L23
Collier Cameron A., Duncan D. K., Ehrenfreund P., Foing B. H., Kuntz K. D., Penston M. V., Robinson R. D., Soderblom D. R., 1990, MNRAS, 247, 415
Collier Cameron A. et al., 1999, MNRAS, 308, 493
Donati J.-F., Brown S. F., 1997, A&A, 326, 1135
Donati J.-F., Collier Cameron A., 1997, MNRAS, 291, 1
Donati J.-F., Collier Cameron A., Hussain G., Semel M., 1999, MNRAS, 302, 437
Donati J.-F., Mengel M., Carter B., Marsden S., Collier Cameron A., Wichmann R., 2000, MNRAS, 316, 699
Donati J.-F. et al., 2003a, MNRAS, 345, 1145
Donati J.-F., Collier Cameron A., Petit P., 2003b, MNRAS, 345, 1187
Gray D. F., 1977, ApJ, 211, 198
Guirado J. C. et al., 1997, ApJ, 490, 835
Innis J. L., Thompson K., Coates D. W., Lloyd Evans T., 1988, MNRAS, 235, 1411
Järvinen S. P., Berdyugina S. V., Tuominen I., Cutispoto G., Bos M., 2005, A&A, 432, 657
Jeffers S. V., 2005, MNRAS, 359, 729
Jeffers S. V., Cameron A. C., Barnes J. R., Aufdenberg J. P., Hussain G. A. J., 2005, ApJ, 621, 425
Jeffers S. V., Barnes J. R., Cameron A. C., Donati J.-F., 2006, MNRAS, 366, 667
Kurucz R. L., 1993, CDROM # 13 (ATLAS9 atmospheric models) and # 18 (ATLAS9 and SYNTHE routines, spectral line data base), Cambridge, MA
Kürster M., Schmitt J. H. M. M., Cutispoto G., 1994, A&A, 289, 899
Lanza A. F., 2005, MNRAS, 364, 238
Lanza A. F., Rodonò M., 1999, A&A, 349, 887
Lanza A. F., Catalano S., Cutispoto G., Pagano I., Rodono M., 1998, A&A, 332, 541
Leighton R. B., 1964, ApJ, 140, 1547
Leighton R. B., 1969, ApJ, 156, 1
Marsh T. R., 1989, PASP, 101, 1032
Martin T. J., Davey S. C., 1995, MNRAS, 275, 31
Parker E. N., 1955, ApJ, 122, 293
Petit P., Donati J.-F., Collier Cameron A., 2002, MNRAS, 334, 374
Radick R. R., Lockwood G. W., Skiff B. A., Baliunas S. L., 1998, ApJS, 118, 239
Reiners A., Schmitt J. H. M. M., 2002, A&A, 384, 155
Rüdiger G., Küker M., 2002, A&A, 385, 308
Unruh Y. C., Collier Cameron A., Cutispoto G., 1995, MNRAS, 277, 1145
Vilhu O., Gustafsson B., Walter F. M., 1991, A&A, 241, 167
Vogt S. S., Hatzes A. P., Misch A. A., Kürster M., 1999, ApJS, 121, 547

This paper has been typeset from a TEX/LATEX file prepared by the author.

Downloaded from https://academic.oup.com/mnras/article/375/2/567/1442930 by guest on 15 December 2020